

Chapter 2

Modeling and Interpretation of Hybridization in Coupled Plasmonic Systems

Saïd Bakhti, Nathalie Destouches, and Alexandre V. Tishchenko

Abstract The coupled mode formalism is introduced to provide a phenomenological understanding of the coupling effects in finite systems of particles. Within this approach, a metal nanoparticle can be viewed as an optical resonator and the formation of hybrid modes, resulting from the coupling between particles, can be anticipated. An efficient numerical algorithm is proposed to extract the characteristics (complex poles and amplitudes) of each resonance of the system.

The spectral behavior of the eigen modes of a single metal sphere is analyzed. The redshift and broadening of the different modes with the increase of the particle size and the local refractive index are characterized. Optimal conditions can be found to maximize the particle absorption as well as the near-field enhancement. Sub-radiant and super-radiant hybrid modes of a dimer are identified from the extinction spectrum of each particle. These hybrid modes have different energetic behavior depending on the inter-particle distance, and can then be compared to bounding (attractive) and anti-bounding (repulsive) states. The near-field enhancement resulting from the hybrid mode excitation is maximized by optimizing the dimer geometry and the surrounding refractive index.

The hybrid modes in a quadrumer are identified. For small particles with a reduced coupling via scattering, the system exhibits an anti-crossing behavior of the hybrid modes typical for weakly coupled resonators. When the particles are sufficiently large to induce a strong coupling in the system, the extinction spectrum of the quadrumer present Fano-like resonances, i.e. resonances with an asymmetric line shape. The hybrid modes at the origin of these particular resonances are identified as sub- and super-radiant modes of the system. The sharp Fano-like resonance has a high figure of merit, making such system promising for sensing applications.

Keywords Plasmon resonances • Coupled mode approach • Metal nanoparticles • Hybrid modes • Fano resonances

S. Bakhti • N. Destouches • A.V. Tishchenko (✉)
CNRS, UMR5516, Hubert Curien Laboratory, Saint-Etienne F-42000, France
e-mail: tishchen@univ-st-etienne.fr

2.1 Introduction

Plasmon resonances induced by the electromagnetic excitation of metal nanoparticles are generally associated with the presence of resonance bands in the spectral response of these nanoparticles [1], and lead to an increase in the local electromagnetic field at resonance wavelengths [2]. Each band corresponding to a particular mode of resonance is characterized by its spectral position and width. These spectral characteristics are strongly dependent on the geometry of the particles as well as on their environment. Changes in the resonance bands result in a red shift of the resonance position as well as in a broadening of the bands when the size of the particle or the local refractive index increases.

In general, the optical response of metal nanoparticles is largely dominated by bands of plasmon resonances. As part of a study of the spectral evolution of these different bands based on certain geometric and environmental parameters, it may be more convenient to deal only with resonance parameters (position and width) rather than considering the whole optical spectra. Different methods allow for retrieving these parameters; they are based on Mie theory for spheres [3], the eigenvalues of surface integrals [4], or the hybridization theory for more complex systems [5, 6]. We propose here to develop a method to extract precisely the resonance parameters from the total optical response of a system of particles based on the T-matrix method and its generalization to multi-particle systems [7, 8]. The main objective of this development is to provide an efficient and flexible numerical tool for the characterization of plasmon resonances together with a phenomenological approach to interpret their physical behavior [9–11].

We first introduce the coupled mode model applied to the phenomenological description of the plasmon resonance amplitudes resulting from an external excitation, allowing a treatment of metal nanoparticles as optical resonators. This model is applied to a single resonance mode and extended to a pair of coupled modes, providing a set of phenomenological parameters including losses, coupling with excitation and mutual coupling coefficients. This approach anticipates the formation of hybrid modes as resulting from the coupling between two plasmon modes. The coupled mode model is applied to the complex valued extinction coefficient of the individual particles, defined as an extension of the classical extinction cross-section. This coefficient, having the same phase than the dipolar moment of the particles, appears as a convenient parameter to identify the nature of the hybrid modes in a coupled system. The solutions of the coupled mode equations being in the form of a singular function of the pulsation, we propose an efficient numerical algorithm to extract the characteristics (complex poles and amplitudes) of each resonance of the system from the rigorous computation of complex valued extinction coefficients. All phenomenological parameters describing the coupling between particles can be deduced from these characteristics.

Within this theoretical framework, we first analyze the spectral behavior of the eigenmodes of a single silver sphere. The redshift and broadening of the different modes with the increase of the particle size and the local refractive index are characterized and optimal conditions are found to maximize the particle absorption as well as the near-field enhancement. The case of a silver dimer is then studied,

where sub-radiant and super-radiant hybrid modes are identified from the extinction spectrum of each particle. These hybrid modes have different energetic behaviors depending on the inter-particle distance, and can then be compared to bounding (attractive) and anti-bounding (repulsive) states. Local field enhancement resulting from hybrid mode excitation can be maximized by optimizing the dimer geometry and the surrounding refractive index. Our method is finally applied to silver quadrumers, where hybrid modes exhibit an anti-crossing behavior in the case of weakly coupled small particles. For larger particles, their strong coupling induces the appearance of a Fano-like resonance in extinction spectra. The hybrid modes at the origin of this sharp asymmetric resonance line shape are identified and their behavior is analyzed, showing their potential for sensing applications.

2.2 Coupled Mode Model Applied to Interacting Plasmon Modes

We determine in this section an equation governing the coupled plasmon mode amplitudes, with a few phenomenological parameters characterizing the coupling behavior in simple plasmonic systems. The proposed formalism is well known in the classical coupled mode theory [12] and can be applied to more complex geometries.

A single plasmon mode can be described by a first order differential equation giving the time variations of the mode amplitude $a(t)$ when excited by an incident wave with electric field $f_0(t)$

$$\frac{da(t)}{dt} = -j\text{Re}\{\omega_p\}a(t) - \frac{1}{\tau}a(t) + \kappa f_0(t) \quad (2.1)$$

where τ is the time decay of the plasmon (representing the total losses in the resonant system including absorption as well as re-radiation attributed to scattering), κ is the coupling coefficient and ω_p is the complex resonant angular frequency of the plasmon mode. The real part of ω_p corresponds to the resonance position and the imaginary part to its half width at half maximum (HWHM). When both the incident radiation and the plasmon amplitude oscillate at angular frequency ω , they can be expressed in terms of their modulation amplitudes $\tilde{f}_0(t)$ and $\tilde{a}(t)$ respectively

$$\begin{cases} f_0(t) = \tilde{f}_0(t)\exp\{-j\omega t\} \\ a(t) = \tilde{a}(t)\exp\{-j\omega t\} \end{cases} \quad (2.2)$$

Substituting these expressions into Eq. (2.1) and fixing condition $\tilde{f}_0(t) = 1$ which corresponds to a plane wave with unit amplitude we get the following particular solution of Eq. (2.1) in steady state

$$\tilde{a}(\omega) = \frac{j\kappa}{\omega - \text{Re}\{\omega_p\} + \frac{j}{\tau}} \quad (2.3)$$

Final modulation amplitude \tilde{a} depends on angular frequency ω only and the obtained expression can be written in a very simple form as:

$$\tilde{a}(\omega) = \frac{a_p}{\omega - \omega_p} \quad (2.4)$$

where the coupling coefficient is related with amplitude as $a_p = j\kappa$, and the time decay corresponds to the imaginary part of the complex pulsation $\text{Im}\{\omega_p\} = -1/\tau$. The coupling coefficient quantifies the coupling between the incident excitation and the plasmon mode. Its amplitude provides the coupling strength and its phase corresponds to the oscillator phase at resonance relative to the excitation.

In the case of close particles, plasmon resonances strongly interact, resulting in the formation of hybrid modes in the system. To generalize the phenomenological description to coupled systems, consider first two interacting plasmon modes. One can write two coupled-mode equations on the basis of Eq. (2.1). Two modes with amplitudes $a_1(t)$ and $a_2(t)$ and complex angular eigen frequencies ω_1 and ω_2 are coupled to the incident radiation with coupling coefficients κ_1 and κ_2 . Phenomenological equations managing these modes can be written in the following form:

$$\begin{cases} \frac{da_1(t)}{dt} = -j\text{Re}\{\omega_1\}a_1(t) + \text{Im}\{\omega_1\}a_1(t) + \kappa_1 f_0(t) + \kappa_{12}a_2(t) \\ \frac{da_2(t)}{dt} = -j\text{Re}\{\omega_2\}a_2(t) + \text{Im}\{\omega_2\}a_2(t) + \kappa_2 f_0(t) + \kappa_{21}a_1(t) \end{cases} \quad (2.5)$$

where κ_{12} and κ_{21} are the coupling coefficients between the two modes. The temporal amplitudes of the modes can be expressed in terms of their temporal envelope similarly to the case of a single mode:

$$\begin{cases} a_1(t) = \tilde{a}_1(t)\exp(-j\omega t) \\ a_2(t) = \tilde{a}_2(t)\exp(-j\omega t) \end{cases} \quad (2.6)$$

Substituting expressions (2.6) into Eq. (2.5), we get rid of the fast oscillating term $\exp(-j\omega t)$. The particular solution of the coupled mode equations is found in steady state, when $\tilde{f}_0(t) = 1$:

$$\begin{cases} \tilde{a}_1(\omega) = \frac{a_1^+}{\omega - \omega^+} + \frac{a_1^-}{\omega - \omega^-} \\ \tilde{a}_2(\omega) = \frac{a_2^+}{\omega - \omega^+} + \frac{a_2^-}{\omega - \omega^-} \end{cases} \quad (2.7)$$

The solutions appear as a linear superposition of two singular functions, showing that the coupling between the plasmon modes results in the formation of two hybrid modes with complex resonance angular frequencies ω^+ and ω^- distinct from the original modal angular frequencies. The values of the phenomenological parameters a_1^- , a_1^+ , a_2^- , a_2^+ , ω^+ and ω^- of these hybrid modes can be found by fitting the

optical response of the system with a meromorphic function of the pulsation that has two singular points. All phenomenological parameters introduced in Eqs. (2.5) are then related with the resonance parameters of hybrid modes. The coupling coefficients depend on the polar amplitudes as:

$$\begin{cases} \kappa_1 = -j(a_1^+ + a_1^-) \\ \kappa_2 = -j(a_2^+ + a_2^-) \end{cases} \quad (2.8)$$

Since these coefficients are intrinsic for the given modes, the sum of hybrid mode amplitudes $a_1^+ + a_1^-$ and $a_2^+ + a_2^-$ must remain constant whatever the strength of the coupling between the modes. The mutual coupling coefficients are

$$\begin{cases} \kappa_{21} = -\frac{a_2^+ a_2^-}{a_1^+ a_2^- - a_1^- a_2^+} \Delta\omega^\pm \\ \kappa_{12} = \frac{a_1^+ a_1^-}{a_1^+ a_2^- - a_1^- a_2^+} \Delta\omega^\pm \end{cases} \quad (2.9)$$

with $\Delta\omega^\pm = \omega^+ - \omega^-$. Considering that these coupling coefficients reflect the coupling strength in the system and regarding to their expressions, the difference between the complex angular frequencies of hybrid modes, $\Delta\omega^\pm$, as well as products of their amplitudes give a direct estimate of the coupling effects in particle aggregates. Similarly to the coupling coefficients, the mutual coupling coefficients are complex parameters whose amplitude provides a direct estimate of the coupling strength between the particles, and their phase corresponds to the phase detuning with which one mode acts on the other.

Finally, the initial and hybrid mode angular frequencies are linked as follows:

$$\begin{cases} \omega^+ = \omega_1 + j\frac{a_2^+}{a_1^+}\kappa_{12} \\ \omega^- = \omega_2 + j\frac{a_1^-}{a_2^-}\kappa_{21} \end{cases} \quad (2.10)$$

These relations show that with given initial modes, the shift in hybrid modes depends directly on the mutual coupling coefficients, as expected in strongly coupled oscillators [13].

In the limit of uncoupled modes, e.g. by sufficiently distancing two particles so that they no longer interact with each other, the mutual coupling coefficients nullify and the Eq. (2.5) become independent. In this case, vanishing mode amplitudes a_1^- and a_2^+ ensure that the mutual coupling coefficients become zero and that the hybrid mode angular frequencies tend to the initial values ($\omega^+ \rightarrow \omega_1$ and $\omega^- \rightarrow \omega_2$).

2.3 Definition of the Complex Valued Extinction of Nanoparticle Assemblies

In the general case of a system with interacting particles our strategy is to consider a single parameter characterizing the response of each particle. A practical way to characterize the optical response of a system of particles is to introduce the optical cross-sections [14]. In particular, the extinction cross-section C_{ext} , which expresses the total optical losses in the system due to absorption and scattering processes. In the case of a single particle, this quantity is expressed using the optical theorem:

$$C_{ext} = \frac{4\pi}{k_s |\mathbf{E}_0|^2} \text{Im} [\mathbf{E}_0^* \cdot \mathbf{E}_{sca}^\infty(\mathbf{e}_k)] \quad (2.11)$$

where $\mathbf{E}_{sca}^\infty(\mathbf{e}_k)$ is the far-field scattered in the forward direction \mathbf{e}_k of the incident field. The latter is assumed to be a monochromatic incident plane wave $\mathbf{E}_{inc} = \mathbf{E}_0 \exp(i\mathbf{k}_s \cdot \mathbf{r})$ of angular frequency ω propagating in the homogeneous medium of refractive index n_s with wavevector k_s . For a multi-particle system, the total extinction cross-section can be defined as the sum of the individual particle extinction cross-sections.

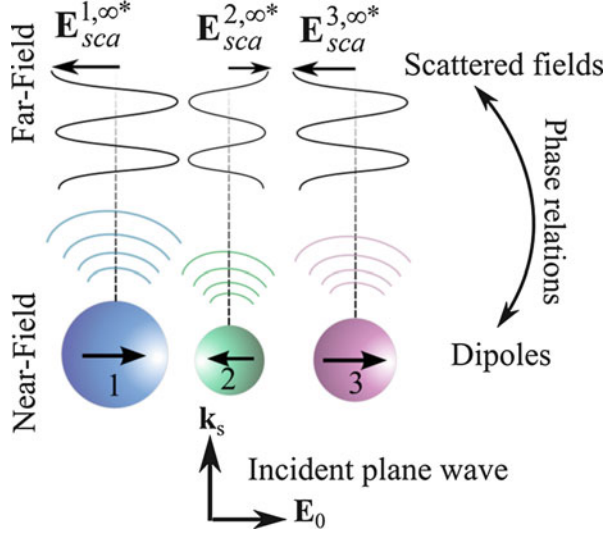
In order to generalize the concept of extinction cross-section, we introduce the complex valued extinction \tilde{C}_{ext}^i for each particle and \tilde{C}_{ext} for the whole system on the basis of the conventional extinction cross-section defined in Eq. (2.11)

$$\tilde{C}_{ext} = \sum_i \tilde{C}_{ext}^i = - \sum_i \frac{4\pi}{k_s |\mathbf{E}_0|^2} \mathbf{E}_0 \cdot \mathbf{E}_{sca}^{i,\infty*}(\mathbf{e}_k) \quad (2.12)$$

where $\mathbf{E}_{sca}^{i,\infty}(\mathbf{e}_k)$ is the far-field scattered by the i^{th} particle. The optical theorem expressed in Eq. (2.11) defines the extinction cross-section as an attenuation of the incident radiation in the forward direction. In contrast to its conventional analogue, the complex valued extinction defined in Eq. (2.12) gives access to the phase information resulting from the interaction of the scattered field with the incident one. Even if the individual contributions \tilde{C}_{ext}^i to the total extinction do not represent any measurable quantity, they allow for characterizing contribution of each particle to the optical response of the whole system. To interpret the resonance curves we study the phase as well as the real and imaginary parts of the individual complex valued extinctions, noting that their imaginary parts correspond to the conventional extinction cross-section. The phase of the complex valued extinction coincides with that of the dipolar moment oscillation.

Complex partial extinctions provide information about relative oscillations of the particle dipole moments. When particles are illuminated with a constant phase of the incident plane wave (Fig. 2.1), the phase difference between their scattering in the far field (and thus between their partial extinction according to Eq. (2.12)) results from a phase difference in their dipolar moments. The complex extinction

Fig. 2.1 Schematic representation of phase relations between partial scattered fields and oscillating dipolar moments of a system of particles (Reprinted with permission from Ref. [10]. Copyright 2015 American Chemical Society)



can therefore be conveniently used to characterize the radiation of each particle in a coupled system.

2.4 Numerical Extraction of Resonance Parameters

We describe the complex extinction coefficient (or each individual contribution to the total extinction) by a meromorphic function of angular frequency ω , with m poles corresponding to m resonances:

$$\tilde{C}_{ext}(\omega) = \sum_{j=1}^m \frac{a_j}{\omega - \omega_j} + \sum_{k=0}^{\infty} b_k \omega^k \quad (2.13)$$

This function is composed of singular and regular parts. Each singular term corresponds to a particular resonance characterized by its complex amplitude a_j and a complex angular frequency ω_j . The real part of the latter corresponds to the spectral position of the resonance and its imaginary part to the HWHM. We propose a numerical algorithm for the determination of the characteristics of each resonance. The different steps of the approach are the following. First, in order to obtain an analytical function without singular function, $\tilde{C}_{ext}(\omega)$ is multiplied by polynomial $P_m(\omega)$ which zeros are the poles of $\tilde{C}_{ext}(\omega)$:

$$P_m(\omega) = \prod_{j=1}^m (\omega - \omega_j) = \sum_{k=0}^m p_k \omega^k \quad (2.14)$$

Then, an $(m+n)^{th}$ order derivation is applied to this product, with $m+n$ being sufficiently large to cancel all the regular terms in (2.13) for $k < n$. The derivation is performed numerically on product $\tilde{C}_{ext}(\omega)P(\omega)$ at $m+n$ discrete values of ω , and by applying the $(m+n)^{th}$ order Newton divided difference formula:

$$\sum_{i=0}^{m+n} \frac{\tilde{C}_{ext}(\omega_i)P_m(\omega_i)}{\prod_{\substack{l=0 \\ l \neq i}}^{m+n} (\omega_i - \omega_l)} = \sum_{k=0}^m p_k \sum_{i=0}^{m+n} \frac{\tilde{C}_{ext}(\omega_i)\omega_i^k}{\prod_{\substack{l=0 \\ l \neq i}}^{m+n} (\omega_i - \omega_l)} \approx 0 \quad (2.15)$$

The relation yields a linear equation on polynomial coefficients p_k considered as unknowns

$$\sum_{k=0}^{m-1} A_k p_k = -A_m \quad (2.16)$$

where

$$A_k = \sum_{i=0}^{m+n} \left[\omega_i^k \tilde{C}_{ext}(\omega_i) \prod_{\substack{l=0 \\ l \neq i}}^{m+n} (\omega_i - \omega_l)^{-1} \right] \quad (2.17)$$

Taking m different sets of $m+n$ couples of points $(\omega_i; \tilde{C}_{ext}(\omega_i))$ leads to a system of m linear equations, whose resolution delivers m polynomial coefficients p_k , $k = 0, 1, 2, \dots, m-1$. The last step consists in searching the roots of polynomial $P_m(\omega)$ defined by coefficients p_k . This can be efficiently done by factorizing the companion matrix \mathbf{C}_m of polynomial $P_m(\omega)$ using the QR algorithm [15]:

$$\mathbf{C}_m = \begin{pmatrix} 0 & 0 & \cdots & 0 & -p_0 \\ 1 & 0 & \cdots & 0 & -p_1 \\ 0 & 1 & \cdots & 0 & -p_2 \\ \vdots & \vdots & \ddots & \vdots & \vdots \\ 0 & 0 & \cdots & 1 & -p_{m-1} \end{pmatrix} \quad (2.18)$$

Each eigenvalue of matrix \mathbf{C}_m is equal to one of the polynomial roots and, consequently, to one of the poles of $\tilde{C}_{ext}(\omega)$.

Once the poles of $\tilde{C}_{ext}(\omega)$ known, the amplitude of each singular term is obtained from the Lagrangian form of the analytical product, using all $N = 2m + n$ discrete points

$$\tilde{C}_{ext}(\omega) \prod_{k=1}^m (\omega - \omega_k) = \sum_{i=0}^N \left\{ \left[\tilde{C}_{ext}(\omega_i) \prod_{k=1}^m (\omega_i - \omega_k) \right] \prod_{\substack{l=0 \\ l \neq i}}^N \frac{\omega_p - \omega_l}{\omega_i - \omega_l} \right\} \quad (2.19)$$

Resonant amplitude a_p is found in the limit $\omega \rightarrow \omega_p$:

$$a_p = \prod_{\substack{k=1 \\ k \neq p}}^m (\omega_p - \omega_k)^{-1} \sum_{i=0}^N \left\{ \left[\tilde{C}_{ext}(\omega_i) \prod_{k=1}^m (\omega_i - \omega_k) \right] \prod_{\substack{j=0 \\ j \neq i}}^N \frac{\omega_p - \omega_j}{\omega_i - \omega_j} \right\} \quad (2.20)$$

The presented algorithm determines efficiently the resonance characteristics, and only few discretization points are required for one searched pole. In practical application, two sets of points can differ by only one single point. Therefore, the algorithm can be implemented by calculating the values $\tilde{C}_{ext}(\omega_i)$ at only $N = 2m + n$ different angular frequencies. The first linear equation is constructed using the $m + n$ first values of $\tilde{C}_{ext}(\omega_i)$, the second equation uses values from the 2^{nd} to the $(m + n + 1)^{th}$, and so on.

After truncation of the infinite series in Eq. (2.13) the equation becomes a rational approximation of the complex extinction function. Formally, it is comparable to the Pade approximation [16] which is designed to approximate analytic functions. We are looking for a decomposition which better fits a meromorphic function near its poles. Therefore, we aim at the most accurate search of complex poles ω_j and amplitudes a_j , and apply the algorithm based on the numerical derivation [17] instead of conventionally used Baker's algorithm designed for the best analytic function approximation in a fixed spectral interval.

In the simplest case of a single resonance present in the extinction spectrum, the complex pole ω_p related to this resonance can be directly expressed as function of N discrete values of the complex extinction. Then, taking Eq. (2.15) with $P_m(\omega) = \omega - \omega_p$, it follows immediately:

$$\omega_p = \left[\sum_{i=0}^N \frac{\tilde{C}_{ext}(\omega_i)}{\prod_{\substack{j=0 \\ j \neq i}}^N (\omega_i - \omega_j)} \right]^{-1} \sum_{i=0}^N \frac{\omega_i \tilde{C}_{ext}(\omega_i)}{\prod_{\substack{j=0 \\ j \neq i}}^N (\omega_i - \omega_j)} \quad (2.21)$$

Amplitude a_p of a single mode is found as

$$a_p = \sum_{i=0}^N \left[\tilde{C}_{ext}(\omega_i) (\omega_i - \omega_p) \prod_{\substack{j=0 \\ j \neq i}}^N \frac{\omega_p - \omega_j}{\omega_i - \omega_j} \right] \quad (2.22)$$

In the following examples, the extinction coefficients are computed at N equidistant wavelengths in a spectral range containing all searched resonances. Computations

on various systems showed that accurate results (i.e stable resonance poles and amplitudes) are obtained within a number of discrete points only a little larger than the number of poles searched: generally from 3 for a single mode and 5 for two or three modes, to about 15 for about ten modes.

Examples demonstrating capabilities of the method are presented in Fig. 2.2. The extinction coefficient of a silver sphere in vacuum is calculated using the Mie theory and a modified Drude model to fit the metal dielectric permittivity (the used parameters are the same as in Ref. [10]). The plots of extinction denote the presence of a single dipolar resonance in the case of a 10 nm in radius particle (Fig. 2.2a) and both dipolar and quadripolar resonances for a 40 nm in radius particle (Fig. 2.2b). In these two cases, the parameters of equation (2.13) are found using only three discrete points around the single resonance and six points for the particle exhibiting two resonance modes. The singular part is also plotted to demonstrate that the optical response of this system is mainly resonant. The difference between the total extinction and its singular part correspond to the regular part of the meromorphic function (2.13). This regular part, which only adds a slow-varying real part of the extinction, corresponds to non-resonant contributions to the total extinction. Since our analysis is focused on the purely resonant response of metal particles, this regular part will be neglected. Another possibility contained in Eq. (2.13) is to separate the contribution of each mode to the total extinction, as shown in Fig. 2.2c where the extinction due to both dipolar and quadripolar resonance modes are given.

In the context of the physical interpretation of plasmon resonances and their coupling behavior, the proposed method not only allows to compute the resonant parameters of plasmons modes, but also to determine the phenomenological quantities introduced in a previous section. This extraction method combined to the coupled mode model provides a powerful tool to analyze and interpret the resonant effects in coupled systems.

2.5 Eigenmodes of Single Spheres

The polar decomposition of the complex extinction previously described is applied to analyze the resonant behavior of a single silver sphere when its radius R varies. We can note here that different strategies can be adopted for the determination of resonant parameters in the case of a single particle. Since the contribution of each mode to the total extinction can be treated separately by considering the different electric modes in the spherical wave decomposition of the scattered field, the analysis can be efficiently performed by searching a single resonance on each electric mode instead of dealing with several modes in the total extinction of the particle.

Position and width variations of the dipolar resonance are shown in Fig. 2.3a–b versus the particle radius for different refractive indexes of the surrounding medium. These results are in perfect agreement with those obtained in a previous

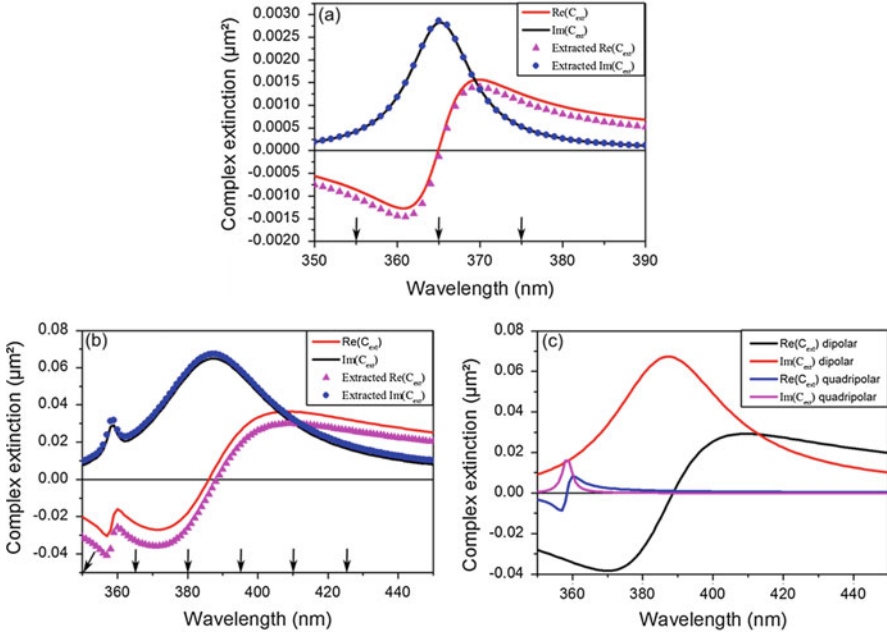


Fig. 2.2 Complex extinction coefficient of a single silver sphere of (a) 10 nm in radius and (b) 40 nm in radius, with its singular part reconstructed after the extraction of resonant characteristics. Arrows indicate the wavelengths used for the extraction algorithm. The dipolar and quadrupolar contributions to the total extinction in the case of a 40 nm in radius particle are given in (c) (Reprinted with permission from Ref. [11]. Copyright 2015 Springer)

numerical study [9]. The resonance position (Fig. 2.3a) is monotonically red-shifted by increasing the sphere radius or the surrounding refractive index n , with a nearly linear dependence of the wavelength position with n (at constant sphere radius). The dipolar resonance bandwidth also exhibits a nearly linear dependence with the ambient refractive index. Its variations versus the particle radius (Fig. 2.3b) meanwhile shows that the bandwidth passes by a minimum value at a radius between 10 and 15 nm depending on the surrounding refractive index. Since this resonance bandwidth can be physically related to the damping strength of the resonance mode due to the absorption and radiative losses, we can deduce that there is an optimal particle size for which the total losses of a given mode are minimal. This optimal particle size is reduced when increasing the local refractive index, from $R = 15$ nm for $n = 1$ to $R = 10$ nm for $n = 2$. The same resonant behavior is observed for higher order modes. As shown in Fig. 2.3c–d, the quadrupolar mode resonates at lower wavelength than the dipolar one, with a lower bandwidth and exhibits minimal losses for higher particle radii.

Once the resonance characteristics are found for a given plasmon mode, we propose to determine the contribution of this mode to the optical cross-sections. To do this within the Mie theory, we remind that the l^{th} plasmon mode cross-sections are easily obtained by considering the l^{th} Lorentz-Mie coefficient corresponding to

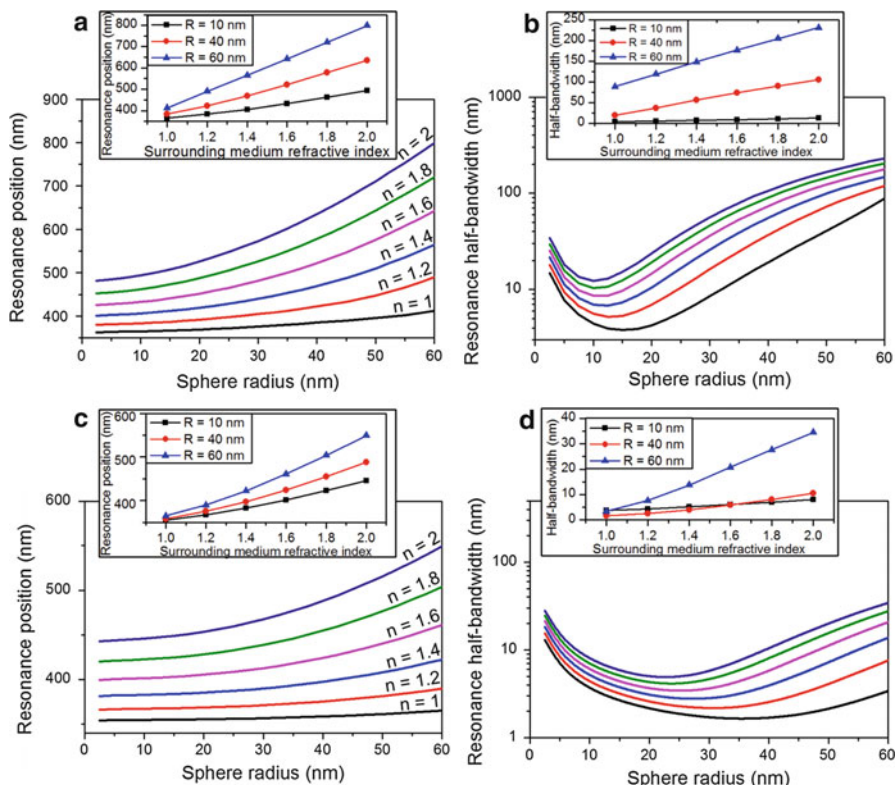


Fig. 2.3 (a) Position and (b) half-bandwidth of the dipolar resonance computed for a single silver sphere versus its radius, for various surrounding medium refractive indexes n . (c) Position and (d) half-bandwidth of the quadrupolar resonance computed for a single silver sphere versus its radius, for various surrounding medium refractive indexes n (Reprinted with permission from Ref. [11]. Copyright 2015 Springer)

electric modes instead of their infinite sum. The absorption, scattering and extinction cross-sections computed at the resonance wavelength of the dipolar and the quadrupolar modes are given in Fig. 2.4a and d in function of the particle radius. It appears that a sphere radius of $R = 22$ nm gives a maximum absorption cross-section and in the same time corresponds to the size from which the scattering cross-section becomes greater than the absorption. This particular behavior is observed whatever the mode and the value of the surrounding refractive index. It then appears that an optimal absorption coincides with equal absorption and scattering cross-sections. This result has been pointed out in the case of point dipoles [18] and for realistic particles [19]. In Ref. [19], the following condition has been established to obtain the l^{th} plasmon resonance mode of a sphere as an ideal absorber:

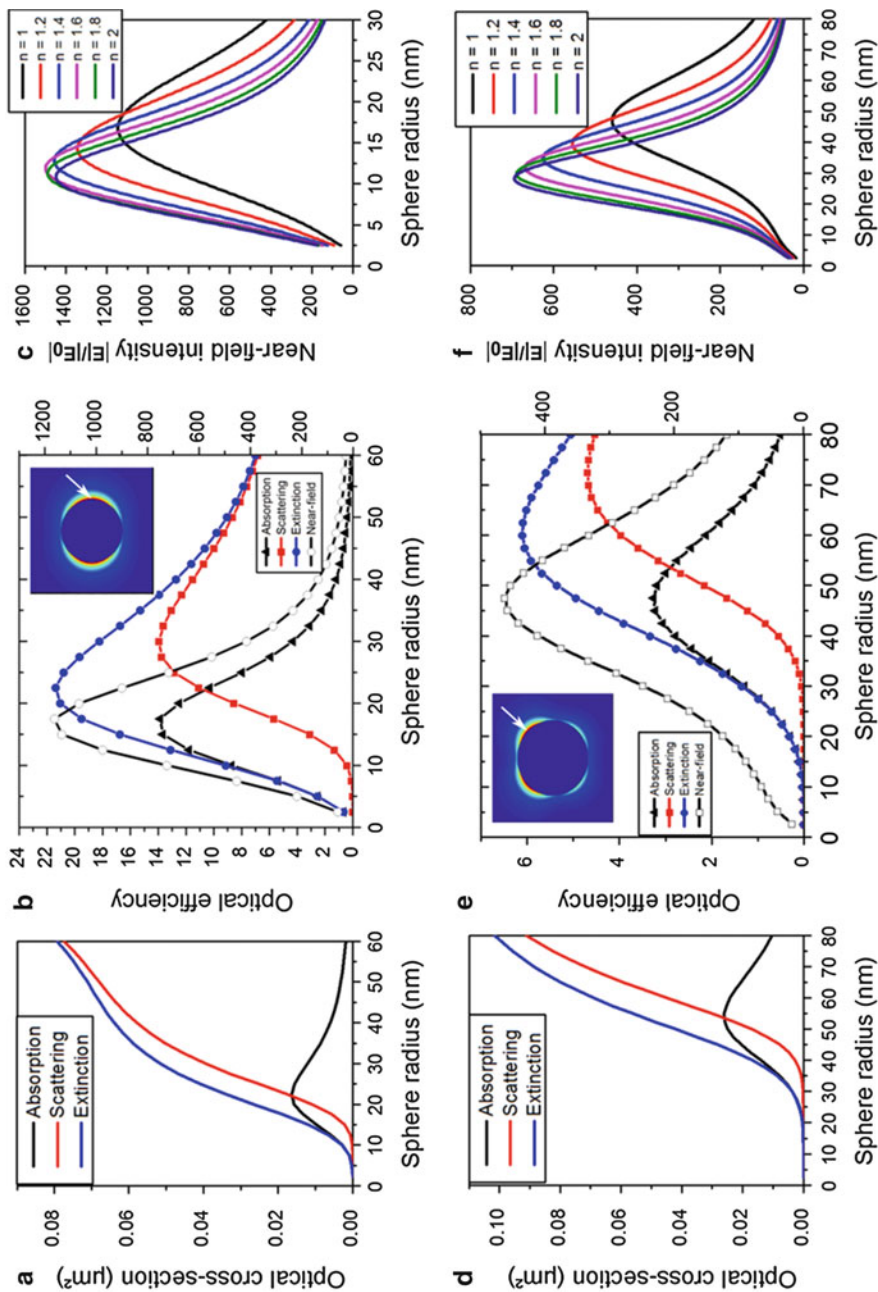


Fig. 2.4 Optical cross-sections of the (a) dipolar and (d) quadrupolar modes of a silver sphere in vacuum versus radius. Optical efficiencies and maximum near-field intensity of (b) the dipolar and (e) quadrupolar modes around the particle in vacuum (at the point indicated by the *white arrow* in the near field intensity mapping given in insets and obtained by illuminating a 17 (40) nm in radius sphere at the dipolar (quadrupolar) resonance position with an horizontally polarized and vertically travelling plane wave). Maximum near-field intensity versus radius for various surrounding refractive indexes, for (c) the dipolar mode and (f) the quadrupolar mode (Reprinted with permission from Ref. [11]. Copyright 2015 Springer)

$$\frac{\varepsilon_1 \tilde{j}_l(k_2 R)}{\varepsilon_2 j_l(k_2 R)} - \frac{\tilde{h}_l^{(1)}(k_1 R)}{h_l^{(1)}(k_1 R)} = 0 \quad (2.23)$$

where $j_l(x)$ is the spherical Bessel function, $h_l^{(1)}(x)$ is the spherical Hankel function of the first kind, \tilde{j}_l and $\tilde{h}_l^{(1)}$ are the derivatives $\tilde{j}_l(x) = [xj_l(x)]'$ and $\tilde{h}_l^{(1)}(x) = [xh_l^{(1)}(x)]'$. ε_1 and k_1 are the dielectric permittivity and the wavenumber of the surrounding medium, ε_2 and k_2 are the dielectric permittivity and the wavenumber of the particle. For a fixed permittivity of the ambient medium and particle, and considering the wavenumbers at resonance position depending on the sphere radius, the condition (2.23) is never strictly satisfied but it has been verified that the optimal absorption of each plasmon mode observed in Fig. 2.4 corresponds to a particle size that minimizes the left-hand of Eq. (2.23).

Other interesting features of the radiative and non-radiative processes at resonance can be drawn from the analysis of the optical efficiencies, i.e. the optical cross-sections normalized by the physical cross-section of the particle (πR^2). Figure 2.4b shows that the absorption and scattering efficiencies for the dipolar mode are maximum for two different radii, $R = 17$ nm and with $R = 30$ nm, respectively. When calculating the maximum near-field intensity produced on the particle surface at dipolar resonance, we observe that its value passes by a maximum in coincidence with the absorption efficiency. This property is quite interesting since it provides an easy way to optimize the near-field enhancement. Complementary calculations prove that variations of the maximum near-field intensity are correlated to variations of the absorption efficiency whatever the considered mode and refractive index of the surrounding medium. Figure. 2.4e–f shows that the sizes for which the optical efficiencies and the maximum near-field intensity of the quadrupolar resonance are maximum, are larger than those calculated for the dipolar resonance and decrease when increasing the surrounding refractive index. Interestingly, the maximum near-field intensity can also be optimized by varying the surrounding refractive index. So, the maximal near-field intensity produced by the dipolar mode is obtained for $n = 1.5$ and $R = 13$ nm.

2.6 Hybrid Modes in Dimers

2.6.1 Hybrid Modes and Their Energetic Behavior

We start the analysis of plasmon modes in dimers by first considering two spheres of 20 nm (S1) and 10 nm (S2) in radius, with a gap of 5 nm between their surfaces and illuminated by a plane wave polarized parallel to the dimer axis. These particles are small enough to mainly exhibit a dipolar resonance when taken separately. We compute separately, from the rigorous resolution of the multiple scattering problem,

the partial complex extinctions \tilde{C}_{ext}^1 and \tilde{C}_{ext}^2 of S1 and S2. Each of these complex quantities exhibits two resonances expected to correspond to hybrid modes resulting from the coupling between the dipolar modes of particles. Fitting their spectral variations with a meromorphic function (being the sum of two singular functions), as described in Eq. (2.7), gives the values of the hybrid pulsations ω^+ and ω^- and amplitude parameters a_1^- , a_1^+ , a_2^- and a_2^+ (Fig. 2.5a). The reconstruction of each singular function of Eq. (2.7) from the extracted parameters is shown in Fig. 2.5c–d. These curves correspond to the contribution of each particle to each hybrid mode. The sum of all these functions, which corresponds to the total complex valued extinction of the system, is compared to the spectral variations calculated rigorously in Fig. 2.5b. The good agreement between the curves proves that the phenomenological approach is accurate for this system.

Looking at the separated contributions of S1 and S2 to each hybrid mode in Fig. 2.5c–d also inform on the nature of these modes. When the phase of the singular functions corresponding to S1 and S2 are the same their mode can be interpreted as resulting from dipoles oscillating in phase (Fig. 2.5c). We can note here that the same sign of the real and imaginary part of the singular functions can also be interpreted as in phase dipolar oscillations. This results in a large dipolar moment and a highly radiative system whose mode is qualified of super-radiant. When the real or the imaginary parts have opposite signs (Fig. 2.5d), the dipolar moments of both particles oscillate out-of-phase leading to a small resulting dipolar moment of the dimer and to a poorly radiative system. The mode is then said sub-radiant. The resonance bandwidth of a given mode is related to the total losses in the system. In the case of a sub-radiant mode, the reduced resulting dipolar moment results in lower radiative losses, leading to a sharper resonance bandwidth. For a super-radiant mode the opposite effect is observed, and the highly radiative behavior results in high radiative losses and hence to a broader resonance bandwidth. These behaviors appear in the two hybrid modes of the dimer.

Similar results are obtained when considering an incident polarization perpendicular to the dimer axis, where both sub-radiant and super-radiant modes are identified from the fitted resonance characteristics.

An important feature in coupled systems is the dependence of the coupling strength with the distance separating the particles. Following the phenomenological analysis in the previous section, the mutual coupling coefficients can serve to quantify the interaction between nanoparticles. Figure 2.6 depicts the modulus of both coupling and mutual coupling coefficients as a function of the gap between the particles, for an incident polarization parallel or perpendicular to the dimer axis. Coupling coefficients κ_1 and κ_2 are intrinsic characteristics of each sphere and then are expected to be independent of the dimer configuration. However, the plotted values show a slight decrease of these coefficients with increasing the gap. This can be interpreted as a consequence of coupling between dipolar modes and higher order modes. Indeed, the phenomenological analysis of the system only consider the ideal case of coupling between two (here dipolar) modes. Actually, coupling

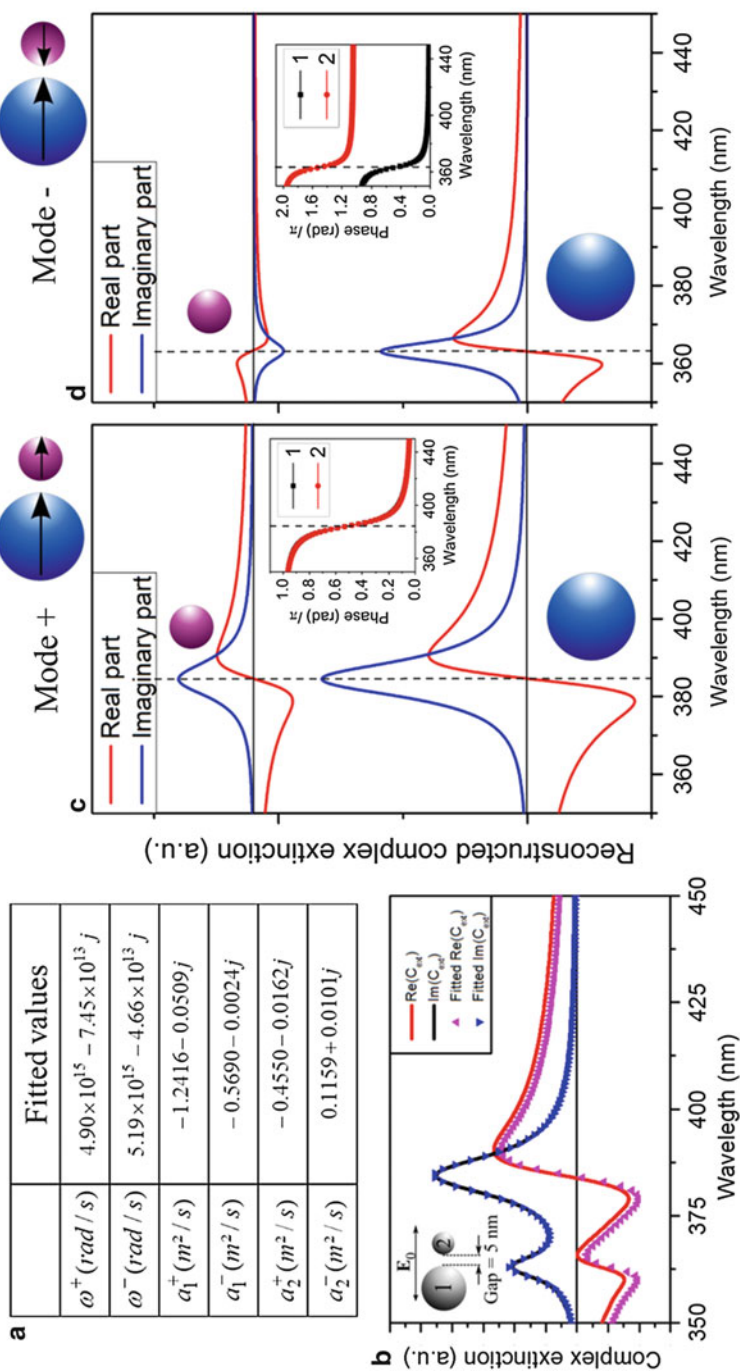


Fig. 2.5 (a) Resonance characteristics of hybrid modes for a dimer composed of 20 and 10 nm in radius spheres, with a gap of 5 nm (b) Comparison of the total complex extinction cross-sections calculated from a rigorous approach and from singular functions of e-d. (c) and (d) Contribution of each particle to the extinction of each hybrid mode (these two graphs have the same ordinate amplitude) (Reprinted with permission from Ref. [10]. Copyright 2015 American Chemical Society)

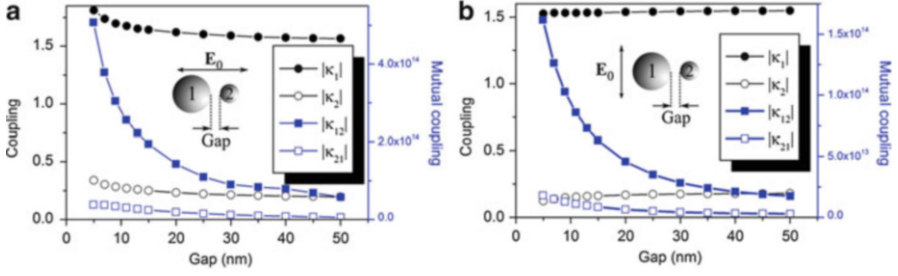


Fig. 2.6 Coupling (on the left y-axis) and mutual coupling (on the right y-axis) coefficients versus the gap between particles for an incident polarization (a) parallel or (b) perpendicular to the dimer axis (Reprinted with permission from Ref. [10]. Copyright 2015 American Chemical Society)

between dipolar and quadrupolar modes also occurs, inducing disparities between expected and computed phenomenological values.

The computed mutual coupling coefficients κ_{12} and κ_{21} show for each incident polarization a fast decreasing coupling strength when increasing the gap between particles. By comparing the amplitudes for each polarization, the coupling strength in the case of a parallel polarization appears to be larger (by a factor of about 3) than in the perpendicular case. When considering each sphere as oscillating dipoles, this result indicates a better coupling in the case of parallel dipolar moments. Regarding again the coupling coefficients, their values are more perturbed for a parallel incident polarization. In this case and for close particles, relatively strong coupling effects can be expected between dipolar and higher order modes, compared with a perpendicular polarization where the coupling coefficients are more stable.

We can note here the different orders of magnitude between the coupling and mutual coupling coefficients. This difference comes from the different physical inputs to which they apply: $\kappa_1 f_0(t)$, $\kappa_2 f_0(t)$, $\kappa_{12} a_2(t)$ and $\kappa_{21} a_1(t)$. These terms have the same dimension and their comparison could inform about the relative importance of the coupling and mutual coupling effects in the resonant behavior of the system.

The hybrid modes resulting from the coupling between particles resonate at complex pulsations ω^+ and ω^- different from the pulsation of initial modes ω_1 and ω_2 . Their determination gives an energetic diagram of the system, as shown in Fig. 2.7a. The latter highlights different behaviors of hybrid modes. The two modes resonating at higher wavelengths (and lower energy) are red-shifted when increasing the inter-particle coupling. They correspond to an energetically favorable configuration of the dipolar moments of the particles, *i.e.* when the dipoles are attractive. These modes can be seen as bounding states of the system (Fig. 2.7c). The modes resonating at lower wavelengths correspond to a repulsive configuration of dipoles and can be seen in turn as anti-bounding states of the system. Another interesting feature is that the resonance position of bounding states tends to the dipolar mode position of the larger particle, whereas the resonance position of anti-bounding states tends to dipolar mode position of the smaller particle.

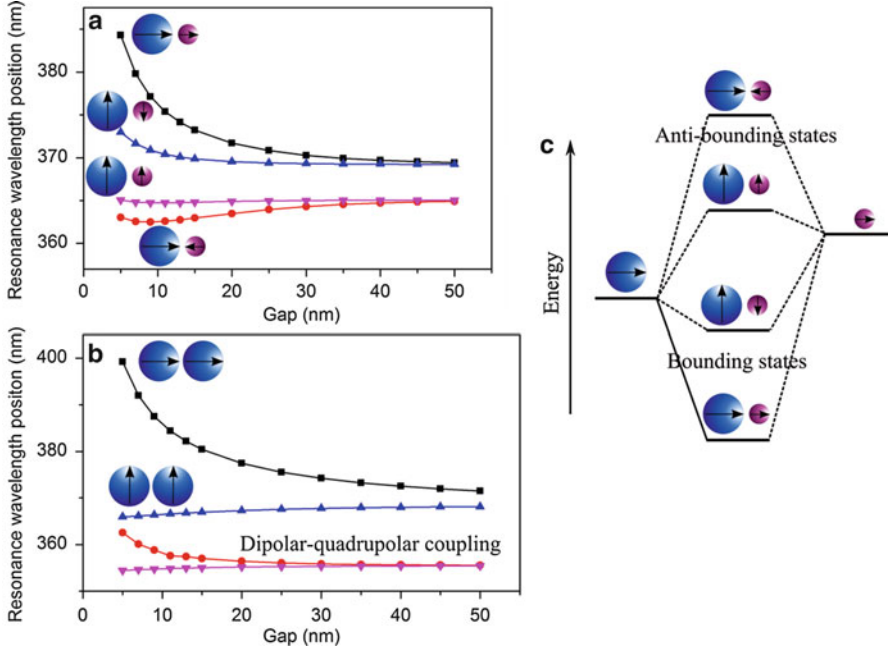


Fig. 2.7 Resonance position of hybrid modes versus the gap between particles for a dimer composed of (a) 10 and 20 nm in radius spheres and (b) identical spheres 20 nm in radius. (c) Schematic representation of the energetic repartition of hybrid modes (Reprinted with permission from Ref. [10]. Copyright 2015 American Chemical Society)

Consider now the special case of homo-dimers, composed of identical particles. In such a case, the initial modes have identical coupling coefficients κ_0 with the incident excitation and resonate at the same pulsation ω_p . Anticipating the mutual coupling coefficients to be equal ($\kappa_{12} = \kappa_{21} = \kappa$) as well as the mode amplitudes ($a_1(t) = a_2(t) = a(t)$) the coupled mode equations (2.5) can be simplified in a single equation:

$$\frac{da(t)}{dt} = -j\text{Re}\{\omega_p\}a(t) + \text{Im}\{\omega_p\}a(t) + \kappa a(t) + \kappa_0 f_0(t) \quad (2.24)$$

Including in Eq. (2.24) the expression of the mode amplitude given by Eq. (2.4), yields in steady-state with the condition $\tilde{f}_0(t) = 1$

$$\tilde{a}(\omega) = \frac{j\kappa_0}{\omega - \omega_p - j\kappa} = \frac{a^+}{\omega - \omega^+} \quad (2.25)$$

As a consequence, the coupling between two identical particles leads to a single excited hybrid mode with a complex pulsation $\omega^+ = \omega_p + j\kappa$ and a resonance amplitude $a^+ = j\kappa_0$. This hybrid mode has the same amplitude as the initial

mode, and the resonance pulsation is only shifted from the initial position ω_p by the mutual coupling term $j\kappa$. Obviously, the resonant response of both particles is exactly the same and the hybrid mode corresponds systematically to a super-radiant mode (in-phase oscillations). Out-of-phase oscillations of dipolar moments appear as forbidden (*i.e.* dark) modes.

The energetic diagram of a homo-dimer composed of 20 nm in radius spheres is plotted in Fig. 2.7b. In addition to the identified hybrid modes, different modes resulting from a coupling between dipolar and quadrupolar initial modes are also represented. For a complete description of these interactions with higher modes, the phenomenological description used has to be generalized to the case of M cross-coupled modes.

2.6.2 Near-Field Enhancement

Let us characterize the spectral behavior of hybrid modes in a silver homo-dimer. Figure 2.8a provides the optical cross-sections of a silver dimer composed of 10 nm in radius spheres with a gap of 5 nm between the particles and illuminated with an incident plane wave polarized with an angle of 45° relative to the dimer axis. These spectra show the presence of three distinct resonance modes. The mode resonating at the lowest energy is identified as the longitudinal hybrid mode with in-phase oscillation of the dipolar moments oriented along the dimer axis. The second marked peak corresponds in turn to the transverse hybrid mode with in-phase oscillation of dipolar moments oriented perpendicularly to the dimer axis. The third mode, not studied in following, resonating at the highest energy originates from a quadrupolar mode. The resonance position and half-bandwidth of the transverse and longitudinal dipolar hybrid modes are reported in Fig. 2.8b–c in function of the gap between the spheres and for various surrounding medium refractive indexes. As expected from the previous analysis, the parallel hybrid mode is red-shifted and slightly broadened when decreasing the inter-particle distance, and therefore when increasing the coupling strength between the particles. By contrary, the parallel dipolar hybrid mode is blue-shifted and slightly narrowed when decreasing the particle gap between the particles. As in the case of a single particle, the resonance position of each hybrid mode has an almost linear dependence with the variation of the local refractive index.

A particular interest of hybrid modes in coupled particle systems relies on the large near-field enhancement that occurs at resonance compared to a single particle. Especially, the hot-spot resulting from the parallel hybrid mode excitation and located in the dimer gap may reach several thousand times the incident wave intensity. Still considering the same dimer with the same illumination condition, the variation of the near-field enhancement at the gap center, obtained at the longitudinal mode resonance position and for various local refractive indexes is reported in Fig. 2.9a. A maximum field enhancement occurs for $n = 1.5$, which corresponds to the surrounding medium refractive index maximizing the dipolar

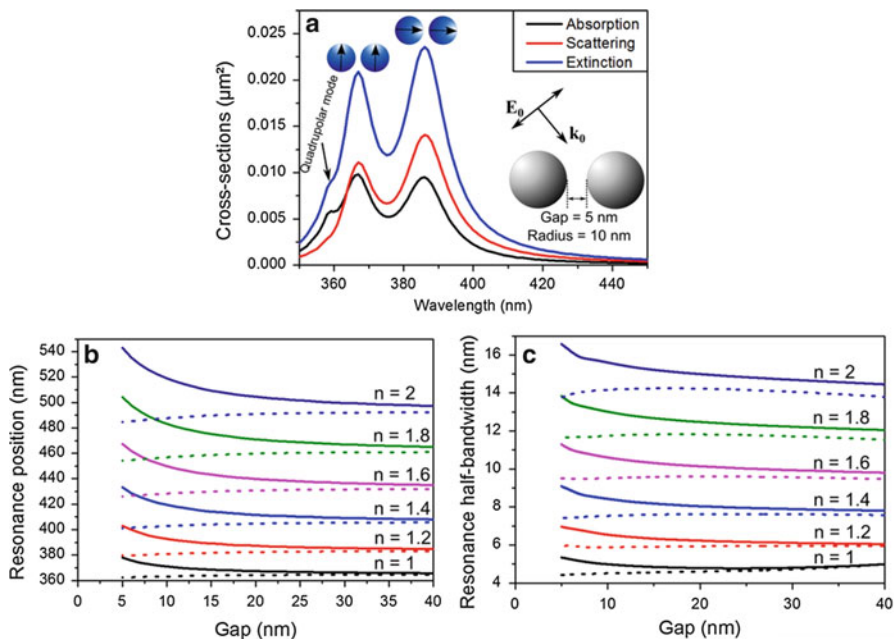


Fig. 2.8 (a) Optical cross-sections of a silver dimer composed of 10 nm in radius spheres with a gap of 5 nm between the particles and illuminated with an incident plane wave polarized with an angle of 45° relative to the dimer axis. The instantaneous dipolar moment orientations of the two dipolar hybrid modes are represented on their respective resonance peak. Resonance (b) position and (c) half-bandwidth of the dipolar hybrid modes versus the gap between the particles, for different local refractive indexes. *Solid lines* correspond to the longitudinal hybrid mode and *dotted lines* correspond to the transverse one (Reprinted with permission from Ref. [11]. Copyright 2015 Springer)

mode near-field intensity for a single particle. As in the same way as for uncoupled modes, the local field enhancement varies when considering different particle sizes. Figure 2.9b plots the near-field intensity for various particle sizes and local refractive indexes, keeping the ratio $R/\text{gap} = 2$. An optimal condition to optimize the hot-spot intensity is then found for $R = 11$ nm and $n = 1.5$.

2.7 Weak and Strong Coupling in Quadrumers

2.7.1 Weak Coupling in Small Size Systems

Here we consider a quadramer composed of two pairs of homo-dimers. This system is schematically described in Fig. 2.10. The first dimer D1 is composed of two 20 nm in radius spheres disposed vertically with a gap of 20 nm. The second dimer

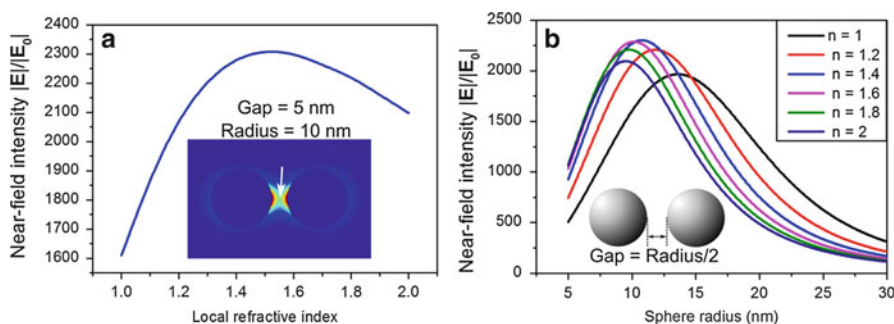
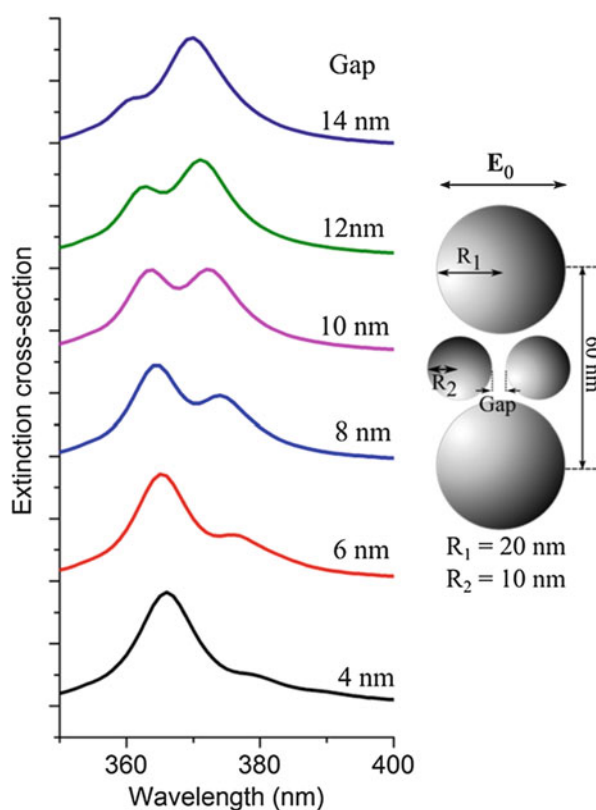


Fig. 2.9 (a) Near-field enhancement versus the local refractive index, at the gap center (shown in inset) of a dimer composed of 10 nm in radius spheres with a gap of 5 nm between the particles and obtained at the longitudinal hybrid mode resonance position and for various local refractive indexes. (b) Near-field intensity versus radius for different surrounding medium refractive indexes. The ratio between the particle radius and the gap is kept equal to 2. In all cases, the incident plane wave is polarized with an angle of 45° relative to the dimer axis (Reprinted with permission from Ref. [11]. Copyright 2015 Springer)

Fig. 2.10 Extinction cross-section of the system sketched on the right composed of two interacting dimers, versus the gap of the horizontal dimer (Reprinted with permission from Ref. [10]. Copyright 2015 American Chemical Society)



D2, composed of two 10 nm in radius spheres disposed horizontally, is placed in the gap of D1. When illuminating this system with an incident plane wave polarized along the D2 axis, the original dimer modes are strongly coupled. The original mode in each dimer results in one hybrid mode where the spheres composing the dimer act as dipoles oscillating in-phase, with dipolar moments oriented parallel to the incident polarization. Then each dimer can be viewed as a single dipole with a given resulting dipolar moment.

The rigorously calculated extinction spectra are plotted in Fig. 2.10 versus the gap of D2. Two hybrid modes appear in the extinction cross-section. As in the case of simple dimers, the coupling between the two dimer modes leads to the formation of hybrid modes with distinct resonance positions.

In order to determine the coupling characteristics of such a quadrumer, we compute the partial complex extinction cross-sections of each dimer \tilde{C}_{ext}^{D1} and \tilde{C}_{ext}^{D2} . As expected, each partial cross-section exhibits two modes located at the same pulsations, which can be fitted with the meromorphic functions of Eq. 2.7. The resonance parameters of the hybrid modes (for a gap of 8 nm in D2) are gathered in Fig. 2.11a and the reconstructed singular functions corresponding to the contribution of each dimer to both hybrid modes are shown in Fig. 2.11c–d. The sum of all these contributions, deduced from the phenomenological approach, is in good agreement with the total complex valued extinction cross-section calculated rigorously (Fig. 2.11b). This proves the validity of the coupled-mode approach for this kind of system too.

As previously, the nature of hybrid modes can be identified through the phase shifts between the dipolar oscillations deduced from the comparison of the sign of the real part of singular functions plotted in Fig. 2.11c–d. For the hybrid mode resonating at pulsation ω^- , the dipolar modes associated to D1 and D2 oscillate in phase (Fig. 2.11c). This hybrid mode corresponds therefore to a high resultant dipolar moment making this mode highly radiative and can be qualified as super-radiant. The hybrid mode resonating at ω^+ is characterized by a $\pi/3$ phase shift between the dipolar oscillations of the two dimers. This configuration is less radiative than a super-radiant mode, and then will be qualified as a sub-radiant mode.

When decreasing the gap between particles in D2, the resonance position of the dimer original mode is red-shifted due to an increase in the coupling strength between particles. This shift changes the position of hybrid resonances. Figure 2.12a shows the energetic diagram of both coupled and isolated dimers in function of the gap in D2. The hybrid modes in the coupled system exhibit an anti-crossing behavior of the energy branches at a gap around 11 nm, where the difference between the two hybrid mode positions presents a minimum. For gaps below 11 nm, the extracted resonance parameters indicate that the super-radiant mode resonates at the lowest wavelengths and conversely for the higher frequency mode. The anti-crossing point induces an energy inversion of the hybrid modes and for higher gaps, the situation is reversed. This behavior is characterized by a sign inversion in the mutual coupling coefficients at crossing point. Since the hybrid

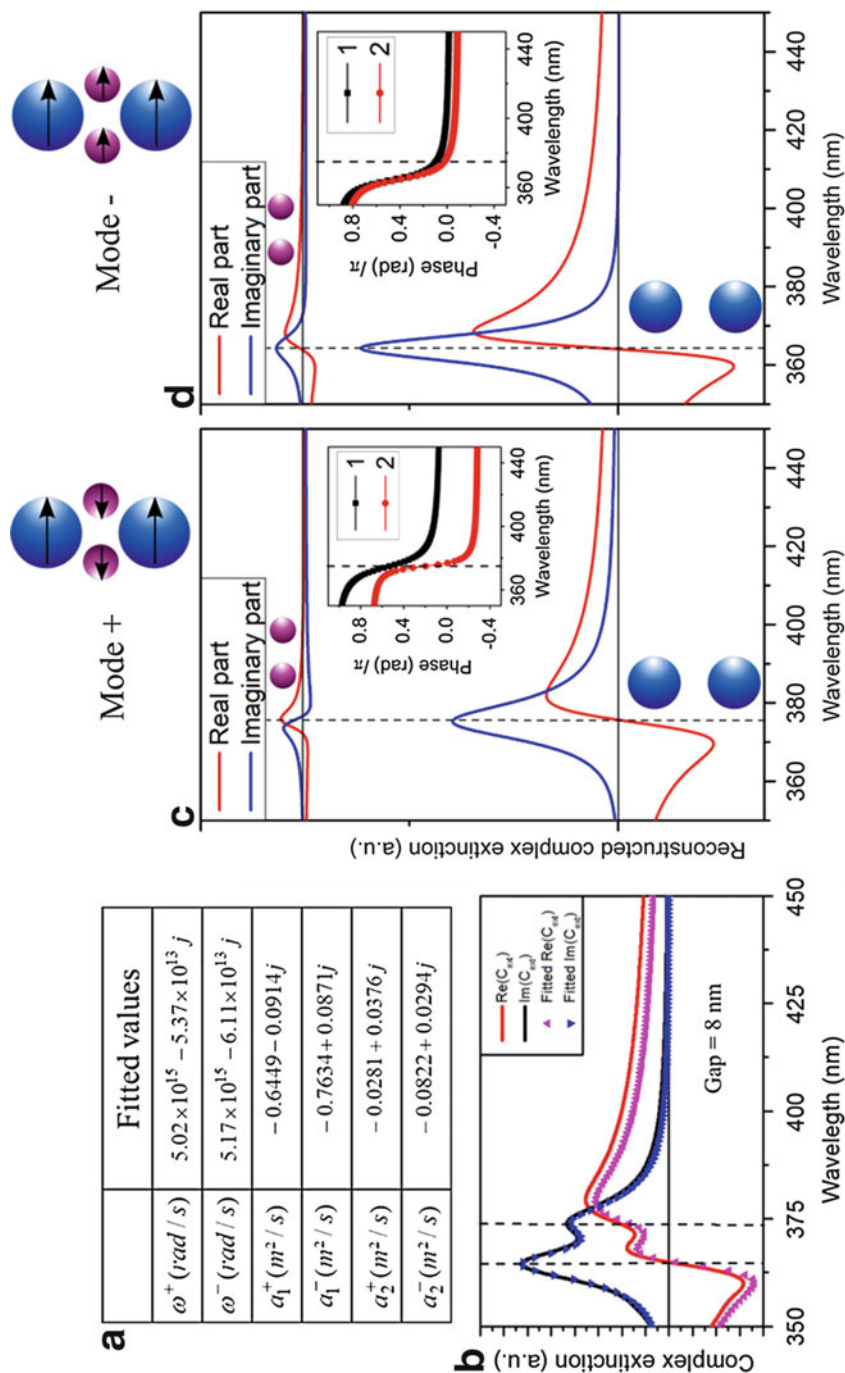


Fig. 2.11 (a) Resonance characteristics fitted from the partial complex valued extinction cross-section of each dimer. The gap of D2 is fixed to 8 nm. (b) Total complex extinction cross-section from rigorous calculation and the phenomenological modeling. (c) and (d) Singular functions giving the contribution of each dimer to each hybrid mode (Reprinted with permission from Ref. [10]. Copyright 2015 American Chemical Society)

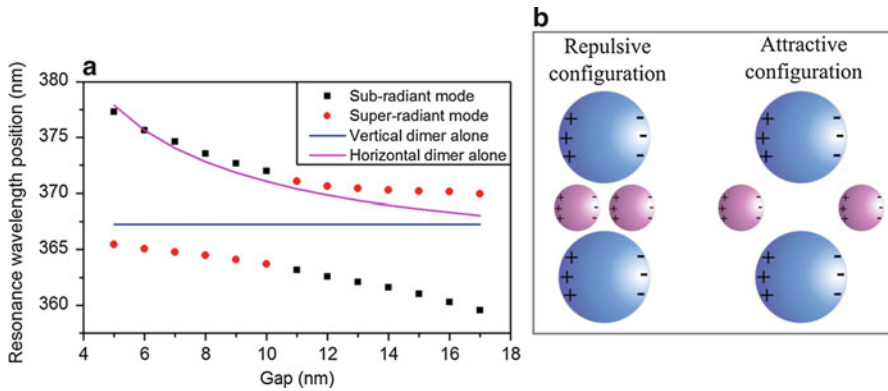


Fig. 2.12 (a) Energetic diagram of coupled and isolated dimers and (b) an illustration of Coulomb interactions between the particles for a small and a large gap of D2 (Reprinted with permission from Ref. [10]. Copyright 2015 American Chemical Society)

pulsations are directly related to these mutual coupling coefficients (see Eq. (2.10)), a sign inversion in the latter induces an energy inversion in the former. As illustrated in Fig. 2.12b, a qualitative interpretation of the energy inversion is given by considering changes in Coulomb interactions between the particles [20]. For short gaps between the particles in D2, repulsive forces act between D1 and D2 particles. When increasing the gap in D2, the electrostatic interactions are reversed, leading to attractive forces between spheres of D1 and D2.

2.7.2 Hybridization and Fano-Like Resonances in Strongly Coupled Systems

We deal now with a quadramer composed of larger particles where stronger coupling between plasmon modes occurs. This system is schematically described in Fig. 2.13, and consists in a quadramer composed of identical spherical particles 30 nm in radius. As previously, this system can be viewed as a pair of vertical (D1) and horizontal (D2) homo-dimers. The extinction spectra of the quadramer are plotted in Fig. 2.13 versus the gap of D2, when illuminating with an plane wave polarized along the D2 axis. These spectra exhibit Fano resonances, *i.e.* asymmetric resonant line profiles, noting also the presence of a quadrupolar resonance at about 360 nm.

In order to analyze the coupling effects in the quadramer, we consider Eqs. (2.5) extended to four coupled equations to describe the mutual coupling between the four particles. Due to the symmetry of this system and considering the given incident polarization, these equations can be reduced into two coupled equations describing the resonance behavior of the quadramer

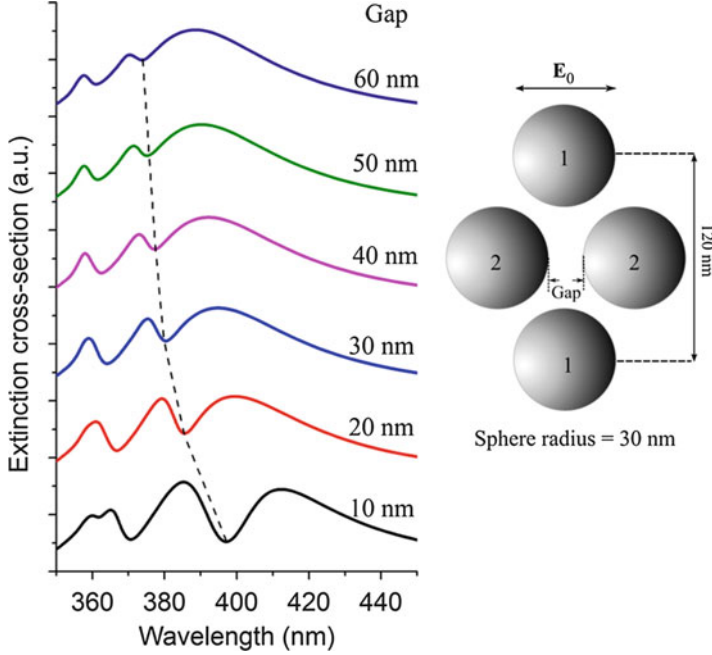


Fig. 2.13 Extinction cross-section of the system sketched on the right composed of two interacting dimers, versus the gap of the horizontal dimer. The *dashed line* indicates the position of the Fano dips in the extinction spectra (Reprinted with permission from Ref. [10]. Copyright 2015 American Chemical Society)

$$\begin{cases} \frac{da_1(t)}{dt} = -j\text{Re}\{\omega_0\}a_1(t) + \text{Im}\{\omega_0\}a_1(t) + \kappa_0 f_0(t) + \kappa_{11}a_1(t) + 2\kappa_{12}a_2(t) \\ \frac{da_2(t)}{dt} = -j\text{Re}\{\omega_0\}a_2(t) + \text{Im}\{\omega_0\}a_2(t) + \kappa_0 f_0(t) + \kappa_{22}a_2(t) + 2\kappa_{12}a_1(t) \end{cases} \quad (2.26)$$

where $a_1(t)$ and $a_2(t)$ are the resonance amplitudes in the dimers D1 and D2, respectively. ω_0 is the original complex pulsation of the particles' dipolar resonance and κ_0 is their coupling coefficient with the incident radiation. κ_{11} and κ_{22} are the mutual coupling coefficients between the particles in the dimers D1 and D2 respectively, κ_{12} is the mutual coupling coefficient between the D1 and D2 particles. The coupled equations (2.26) describing the system anticipates the formation of two different hybrid modes from the coupling of the initial dipolar resonances of the particles.

In order to determine the coupling characteristics of such a quadrumer, we compute the partial complex extinction cross-sections of each dimer \tilde{C}_{ext}^{D1} and \tilde{C}_{ext}^{D2} . The resonance parameters of the hybrid modes (for a gap of 60 nm in D2) are gathered in Fig. 2.14a and the reconstructed singular functions corresponding to

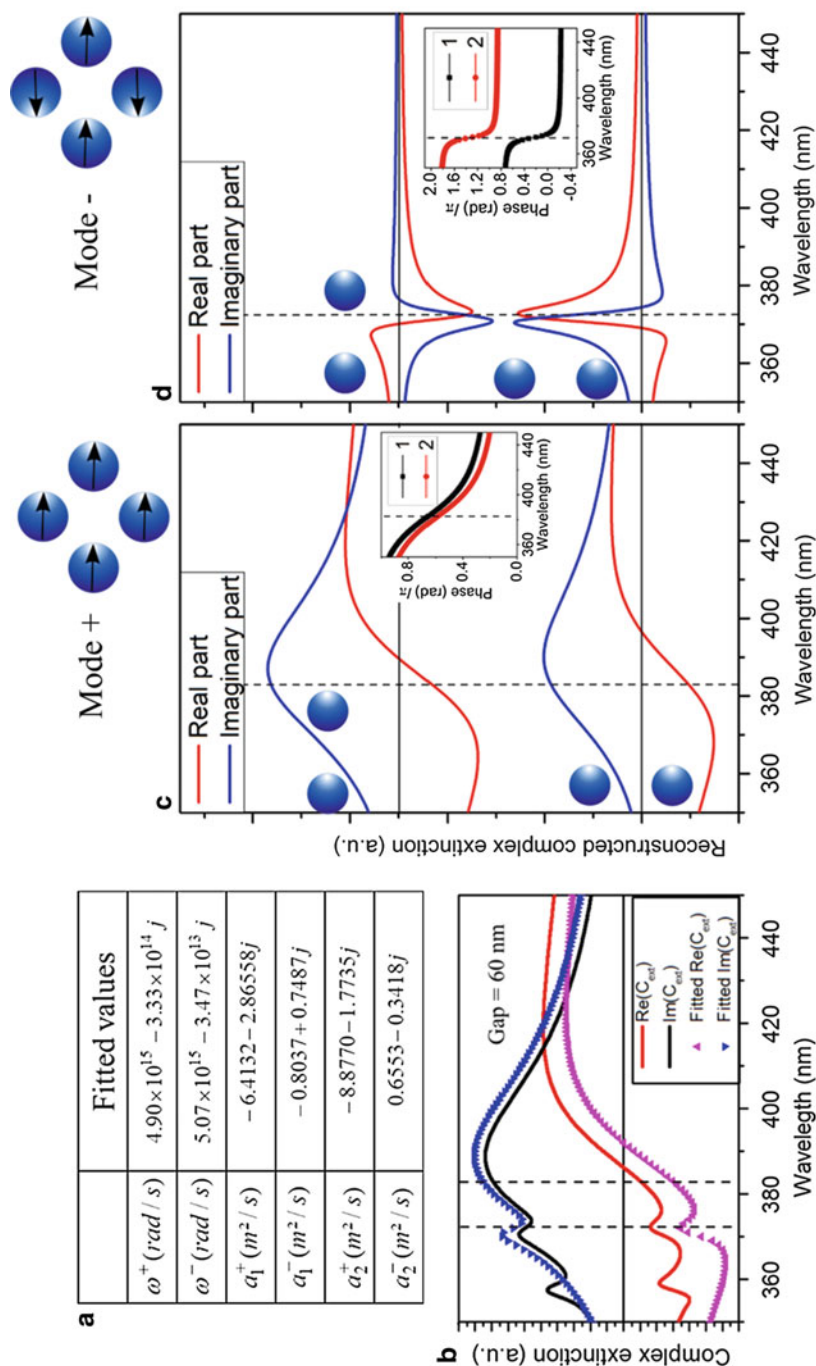


Fig. 2.14 (a) Resonance characteristics fitted from the partial complex valued extinction cross-section of each dimer. The gap of D2 is fixed to 60 nm. (b) Total complex extinction cross-section from rigorous calculation and the phenomenological modeling. (c) and (d) Singular functions giving the contribution of each dimer to each hybrid mode (these two graphs have the same ordinate amplitude) (Reprinted with permission from Ref. [10]. Copyright 2015 American Chemical Society)

the contribution of each dimer to both hybrid modes are shown in Fig. 2.14c–d. The sum of all these contributions, deduced from the phenomenological approach, is in good agreement with the total complex valued extinction cross-section calculated rigorously (Fig. 2.14b), except for the quadrupolar mode (at about 355 nm) not taken into account in our model.

As previously, the nature of hybrid modes can be identified through the phase shifts between the dipolar oscillations deduced from singular functions plotted in Fig. 2.14c–d. For the hybrid mode resonating at angular frequency ω^+ , the dipolar modes associated to D1 and D2 oscillate nearly in phase (Fig. 2.14c). This hybrid mode corresponds therefore to a high resultant dipolar moment making this mode highly radiative and qualified of super-radiant. The hybrid mode resonating at ω^- is characterized by an out-of-phase oscillation of the dipolar moments, making this mode poorly radiative that can be qualified of sub-radiant. A particular feature of this system comes from highly asymmetric line profiles in the contribution of both dimers to the sub-radiant mode. The superposition of these asymmetric line profiles with the contribution of the super-radiant mode explains the Fano line-shape in the total extinction of the quadrumer.

Figure 2.15b shows the plot of relative dipolar moment phases for the two hybrid modes in function of the gap in D2, revealing two different coupling regimes. When increasing the gap between the particles in D2 (corresponding to weak coupling), the super-radiant mode tends to a zero phase shift between all the dipolar moments resulting in a large bandwidth (Fig. 2.15c), and the sub-radiant mode tends to a π phase shift with a reduced bandwidth. This regime results in a sharp Fano resonance in the extinction spectra (Fig. 2.13). In the strong coupling regime, *i.e.* when reducing the gap in D2, a reduction in the phase shifts of the super-radiant mode is observed while its bandwidth is reduced. Contrariwise, the phase difference between the dipolar moments of the sub-radiant mode tends to be reduced and its bandwidth increases. Then under this regime the super-radiant and sub-radiant modes become respectively less and more radiative. Moreover, the plot of the spectral position of these hybrid modes (Fig. 2.13b) shows that the difference between their spectral positions decreases with the gap in D2. The combination of these two modes forms a broader Fano resonance in the structure total extinction spectrum.

An actual interest of Fano resonances in plasmonic structures lies in their extreme sensitivity to the local environment, making such resonances well suited for sensing applications. The sensing capabilities of plasmon resonances can be evaluated through their Figure of Merit [21] (FoM) defined as the ratio of the plasmon energy shift per refractive index unit change in the surrounding medium, divided by the width of the resonance band. Since the FoM of a given mode mainly depends on its spectral width, the Fano resonance of the quadrumer in the weak coupling regime appears as the best configuration for sensing because of its sharp width compared to the Fano resonance in the strong coupling regime. The plot of the quadrumer extinction spectra in the weak coupling regime (Fig. 2.16a) shows the redshift of the asymmetric Fano line profile when increasing the local refractive

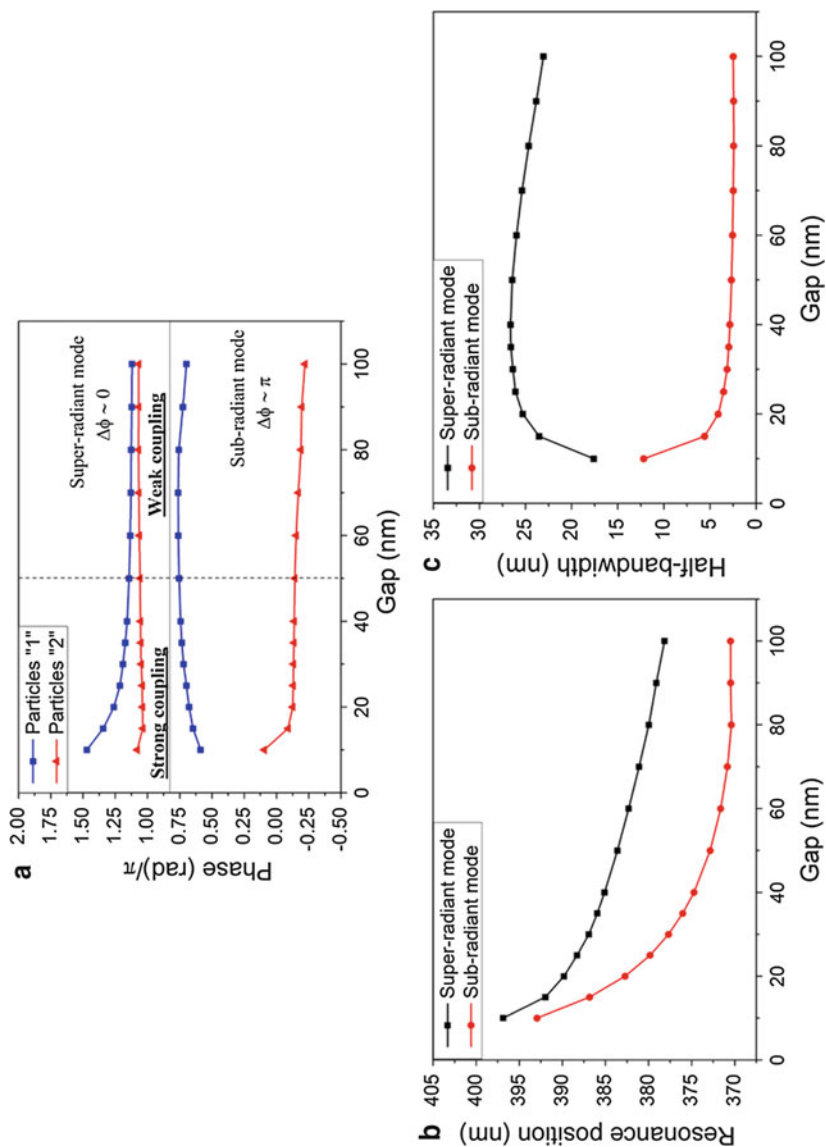


Fig. 2.15 (a) Relative phase between dipolar moment oscillations, (b) resonance position and (c) half-bandwidth of the hybrid mode in the quadrumer versus the gap of the dimer D2 (Reprinted with permission from Ref. [10]. Copyright 2015 American Chemical Society)

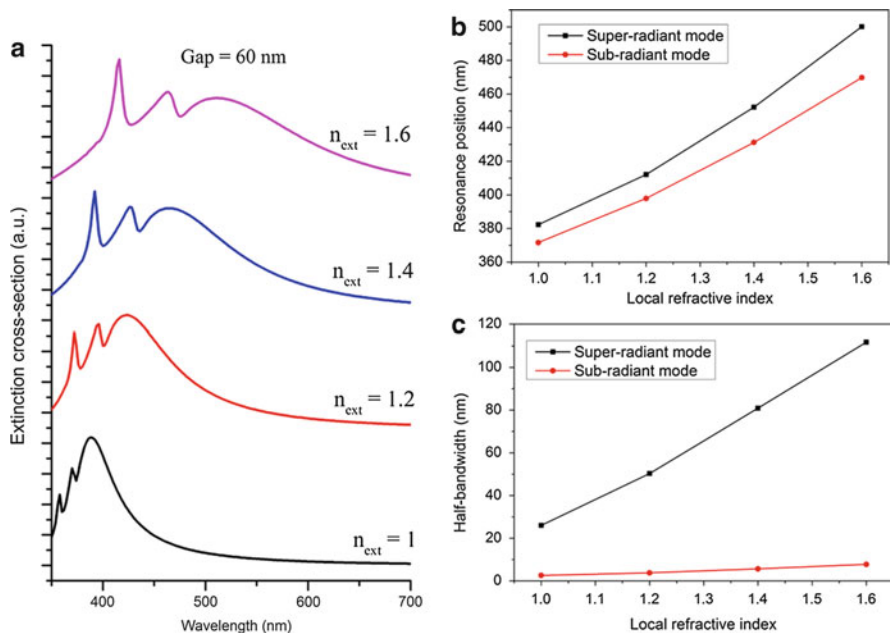


Fig. 2.16 (a) Extinction spectrum of the quadrumer for different surrounding medium refractive indexes. (b) Resonance position and (c) half-bandwidth of the hybrid modes versus the local refractive index. A gap of 60 nm in the dimer D2 is fixed (Reprinted with permission from Ref. [10]. Copyright 2015 American Chemical Society)

index. The plot of the two hybrid modes resonance positions in Fig. 2.16b exhibits a nearly identical energy shift when increasing the surrounding medium refractive index, while the spectral width of the super-radiant mode increases much more significantly than the sub-radiant one (Fig. 2.16c). The latter then retains its low radiative behavior. Using a linear regression of the energy shift versus the local refractive index and the sub-radiant mode FWHM in vacuum, the FoM of the Fano resonance in the weak coupling regime is estimated to 19.4, which is much larger than in previously studied finite structures [22, 23]. By comparison, the FoM in the strong coupling regime is estimated to 6.7, demonstrating the advantage of a weak coupling configuration for sensing applications.

2.8 Conclusion

In this chapter we developed an efficient method for analyzing natural resonant modes of unique particles and their coupling in simple structures. The principle of this method is based on an analytical representation of the optical response of nanostructures, as a unique function of the angular frequency. Thus, each mode of resonance is characterized by a complex pole in the optical response corresponding

to its frequency and amplitude. An extraction algorithm is described first for the determination of the characteristics in the case of single resonances, then it is generalized to the presence of multiple resonances in the extinction spectrum of a multi-particle system.

The analytical representation of singular functions of resonance modes allows to establish phenomenological equations describing these resonances in the time domain. In the case of single particles, temporal modal amplitude can be described through a first-order differential equation with phenomenological parameters realizing losses and coupling with the incident excitation. This approach can also be extended to the interacting modes by introducing a system of coupled equations where mutual coupling terms are involved to account for interaction between modes. The formation of hybrid modes in coupled systems can be predicted according to this formalism.

The method for the extraction of resonance characteristics was first applied to single silver particles with the determination of the position, spectral width and resonance amplitude of eigenmodes of spheres as a function of the sphere radius. Hybrid modes of dimers were then studied. The initial dipole modes of two spheres form in the general case four hybrid modes of the dimer differentiated by the direction of the resulting dipole moment and phase relationships between the oscillations of the dipole moment of each particle. From energetic point of view, these hybrid modes can be seen as bounding and anti-bounding states, characterized by red and blue spectral shifts, respectively, and their resonance positions gives the measure of the power coupling between particles.

Finally, a more complex system consisting of two dimer in interaction was studied. The optical response of this system has asymmetric resonance profiles of Fano type very well taken into account by the singular representation of our model and perfectly characterized by the extraction method.

We conclude that the numerical extraction method of resonance characteristics combined with the phenomenological approach enables efficient characterization and physical interpretation of plasmon resonances and of coupling of their different modes.

References

1. Kreibig U, Vollmer M (1995) Optical properties of metal clusters. Springer Series in Materials Science. Springer, Berlin/New York. doi:[10.1007/978-3-662-09109-8](https://doi.org/10.1007/978-3-662-09109-8)
2. Hao E, Schatz GC (2004) Electromagnetic fields around silver nanoparticles and dimers. *J Chem Phys* 120:357–366. doi:[10.1063/1.1629280](https://doi.org/10.1063/1.1629280)
3. Kolwas K, Derkachova A (2010) Plasmonic abilities of gold and silver spherical nanoantennas in terms of size dependent multipolar resonance frequencies and plasmon damping rates. *Opto-Electron Rev* 18:429–437. doi:[10.2478/s11772-010-0043-6](https://doi.org/10.2478/s11772-010-0043-6)
4. Mayergoyz ID, Fredkin DR, Zhang Z (2005) Electrostatic (plasmon) resonances in nanoparticles. *Phys Rev B* 72:155412. doi:[10.1103/PhysRevB.72.155412](https://doi.org/10.1103/PhysRevB.72.155412)

5. Prodan E, Radloff C, Halas NJ, Nordlander P (2003) A hybridization model for the plasmon response of complex nanostructures. *Science* 302:419–422. doi:[10.1126/science.1089171](https://doi.org/10.1126/science.1089171)
6. Nordlander P, Oubre C, Prodan E et al (2004) Plasmon hybridization in nanoparticle dimers. *Nano Lett* 4:899–903. doi:[10.1021/nl049681c](https://doi.org/10.1021/nl049681c)
7. Mackowski DW (1991) Analysis of radiative scattering for multiple sphere configurations. *Proc R Soc Lond Ser Math Phys Sci* 433:599–614. doi:[10.1098/rspa.1991.0066](https://doi.org/10.1098/rspa.1991.0066)
8. Mackowski D (2012) The extension of Mie theory to multiple spheres. In: Hergert W, Wriedt T (eds) *Mie theory*. Springer, Berlin/Heidelberg, pp 223–256
9. Bakhti S, Destouches N, Tishchenko AV (2014) Analysis of plasmon resonances on a metal particle. *J Quant Spectrosc Radiat Transf* 146:113–122. doi:[10.1016/j.jqsrt.2014.01.014](https://doi.org/10.1016/j.jqsrt.2014.01.014)
10. Bakhti S, Destouches N, Tishchenko AV (2015) Coupled mode modeling to interpret hybrid modes and Fano resonances in plasmonic systems. *ACS Photonics* 2:246–255. doi:[10.1021/ph500356n](https://doi.org/10.1021/ph500356n)
11. Bakhti S, Destouches N, Tishchenko AV (2015) Singular representation of plasmon resonance modes to optimize the near- and far-field properties of metal nanoparticles. *Plasmonics*, 10:1391–1399. doi:[10.1007/s11468-015-9937-y](https://doi.org/10.1007/s11468-015-9937-y)
12. Haus HA (1984) *Waves and fields in optoelectronics*. Prentice-Hall series in solid state physical electronics. Prentice-Hall, Englewood Cliffs
13. Novotny L (2010) Strong coupling, energy splitting, and level crossings: a classical perspective. *Am J Phys* 78:1199–1202. doi:[10.1119/1.3471177](https://doi.org/10.1119/1.3471177)
14. Mackowski DW (1994) Calculation of total cross sections of multiple-sphere clusters. *J Opt Soc Am* 11:2851–2861. doi:[10.1364/JOSAA.11.002851](https://doi.org/10.1364/JOSAA.11.002851)
15. Golub GH, Van Loan CF (1996) *Matrix computations*, 3rd edn. Johns Hopkins University Press, Baltimore
16. Baker GA (1974) *Essentials of padé approximants*. Academic Press, New York
17. Tishchenko AV, Hamdoun M, Parriaux O (2003) Two-dimensional coupled mode equation for grating waveguide excitation by a focused beam. *Opt Quant Electron* 35:475–491. doi:[10.1023/A:1022921706176](https://doi.org/10.1023/A:1022921706176)
18. Tretyakov S (2014) Maximizing absorption and scattering by dipole particles. *Plasmonics* 9:935–944. doi:[10.1007/s11468-014-9699-y](https://doi.org/10.1007/s11468-014-9699-y)
19. Grigoriev V, Bonod N, Wenger J, Stout B (2015) Optimizing nanoparticle designs for ideal absorption of light. *ACS Photonics*. doi:[10.1021/ph500456w](https://doi.org/10.1021/ph500456w)
20. Lovera A, Gallinet B, Nordlander P, Martin OJF (2013) Mechanisms of Fano resonances in coupled plasmonic systems. *ACS Nano* 7:4527–4536. doi:[10.1021/nn401175j](https://doi.org/10.1021/nn401175j)
21. Sherry LJ, Chang S-H, Schatz GC et al (2005) Localized surface plasmon resonance spectroscopy of single silver nanocubes. *Nano Lett* 5:2034–2038. doi:[10.1021/nl0515753](https://doi.org/10.1021/nl0515753)
22. Mirin NA, Bao K, Nordlander P (2009) Fano resonances in plasmonic nanoparticle aggregates†. *J Phys Chem A* 113:4028–4034. doi:[10.1021/jp810411q](https://doi.org/10.1021/jp810411q)
23. Lassiter JB, Sobhani H, Fan JA et al (2010) Fano resonances in plasmonic nanoclusters: geometrical and chemical tunability. *Nano Lett* 10:3184–3189. doi:[10.1021/nl102108u](https://doi.org/10.1021/nl102108u)

Reviews in Plasmonics 2015

Geddes, C.D. (Ed.)

2016, VIII, 453 p. 237 illus., 62 illus. in color., Hardcover

ISBN: 978-3-319-24604-8